ANALYZING THE ANISOTROPY OF THERMAL INFRARED EMISSIVITY OVER ARID REGIONS USING A NEW MODIS LAND SURFACE TEMPERATURE AND EMISSIVITY PRODUCT (MOD21)

V. García-Santos, C. Coll, E. Valor, R. Niclòs and V. Caselles

Department of Earth Physics and Thermodynamics, Faculty of Physics, University of Valencia, 46100 Valencia, Spain.

Corresponding author e-mail: vicente.garcia-santos@uv.es

ABSTRACT

The MOD21 Land Surface Temperature and Emissivity (LST&E) product will be included in forthcoming Moderate Resolution Imaging Spectroradiometer (MODIS) Collection 6. Surface temperature and emissivities for thermal bands 29 (8.55 µm), 31 (11 µm) and 32 (12 µm) will be retrieved using the Advanced Spaceborne Thermal Emission and Reflection Radiometer (ASTER) Temperature and Emissivity Separation (TES) method adapted to MODIS at-sensor spectral radiances, previously corrected with the Water Vapor Scaling method (MOD21 algorithm). We simulated MOD21 product estimates over two different sandy deserts (i.e. White Sands and Great Sands) using a series of MODIS scenes from 2010 to 2013. The objective of this study was to evaluate the anisotropy of the thermal infrared emissivity over semiarid regions, since angular variations of thermal infrared emissivity imply important uncertainties in satellite LST retrievals. The obtained LSEs and their dependence on zenith viewing angles were analyzed. Results from the MOD21 simulated algorithm showed that band 29 LSE decreased up to 0.038 from nadir to zenith angle of 60°, while LSEs for bands 31 and 32 did not show significant variation. MOD21 LSE for band 29 also showed mean differences between night and daytime retrievals of +0.027 for WS and +0.009 for GS. These differences can be attributed to the water vapor adsorption of the soil from the atmosphere. MOD21 nadir and off-nadir LSEs showed a good agreement with laboratory emissivity measurements,

and were used to validate with satellite data a zenithal-dependent emissivity model proposed in a previous study.

KEYWORDS: Emissivity, MODIS, anisotropy, MOD21, TES, angular effects.

1. INTRODUCTION

Land Surface Temperature and Emissivity (LST&E) is one of the most important Earth System Data Records (ESDR's) identified by NASA (King, 1999). LSE, defined as the ratio of the surface emitted radiance to the radiance emitted from a black body at the same thermodynamic temperature (Norman & Becker, 1995), is an intrinsic property of the Earth surface that governs the absorption and emission of energy in the TIR region. Precise and accurate estimates of TIR LSEs are of prime interest to retrieve LST with small uncertainty and bias (Li et al., 2007). LST is an important variable controlling most physical, chemical and biological land processes, useful in several disciplines like agro-meteorology, climatology or hydrology. LST is used, for instance, to study desertification processes, evapotranspiration (Sánchez et al., 2008) or surface-atmosphere interactions (Jacob et al., 2002; Qin et al., 2008).

Many applications can be carried out with the LSE itself, for instance, analyses of land use change (French et al., 2008, Hulley et al., 2014) or land cover characterization (French & Inamdar, 2010). LSE changes with soil moisture content (Mira et al., 2010; García-Santos et al., 2014), type of surface cover (French et al., 2008), surface roughness (Mushkin and Gillespie, 2005), and sensor viewing geometry (García-Santos et al., 2012).

Current remote sensing techniques pursue a maximum uncertainty of ±1 K or less in LST retrievals (Li et al., 2013). Some studies showed errors of ±1 to ±2 K in LST using the single-channel method (Dash et al., 2002). LST errors from the Moderate Resolution Imaging Spectroradiometer (MODIS) generalized split-window (GSW, Wand & Dozier, 1996) are generally within ±1 K for sites with stable atmospheric conditions, except semi-arid and arid regions (Wan and Li 2008, Wan 2014). Uncertainties of ±1 to ±2 K were found for the LST product of the Spinning Enhanced Visible and Infrared Imager (SEVIRI) instrument (Freitas et al., 2010). An average precision of ±1.6 K was found for the LST product of the Geostationary Operational Environmental Satellite R-Series (GOES-R) Program over six different validation sites (Yu et al., 2012). Comparisons between *in situ* LST and the Visible Infrared Imaging Radiometer Suite (VIIRS) derived LSTs showed errors up to ±4 K over arid and semi-arid areas (Guillevic et al., 2014). The Temperature and Emissivity Separation (TES) algorithm (Gillespie et al., 1998) retrieved LST and LSE from the Advanced Spaceborne Thermal Emission and Reflection Radiometer (ASTER) sensor with errors within ±1.5 K and of ±0.005 to ±0.03, respectively (Hulley et al., 2008).

The effect of Thermal Infrared (TIR) emissivity on LST uncertainty is very important. Galve et al. (2008) showed that using the SW algorithm, an emissivity uncertainty of ±0.005 results in a LST uncertainty of ±0.7 K. Hulley & Hook (2009a) showed mean differences for the TIR emissivities from MODIS bands 29 (8.55 μm), 31 (11 μm) and 32 (12 μm) of sand samples collected at the Namib desert (Namibia), of 1.06%, 0.65% and 1.93%, for MOD11B1 versions V4, V4.1 and V5 (Wan, 1999), respectively. The angular dependence on emissivity of land surfaces must be taken into account, since according to Lagouarde et al. (1995), LST measurements for a smooth bare soil at nadir and at 60° showed differences up to 2 K.

In particular, variation of LSE with viewing angle has been shown to be significant in several studies, carried out primarily in field or laboratory conditions. Labed and Stoll (1991) showed that the TIR emissivity of a sand sample does not present angular dependence on the zenith angle up to values greater than 50° and this decrease does not exceed 4.5% for larger zenithal viewing angles. According to Lagouarde et al. (1995), for samples whose texture implies particles size less than 4–5 cm, the effects associated with angular measurements of brightness surface temperature are caused by the anisotropy of the surface emissivity. In

Cuenca and Sobrino (2004), emissivity of a sand sample showed a decrease with zenith angle (θ) of around 2% at spectral ranges 8–14 μm, 11.5–12.5 μm and 10.3–11.3 μm, but presented a pronounced decrease of 5% at 8.2–9.2 μm. Recently García-Santos et al. (2012) and (2014) showed the LSE decrease at large zenith angles (θ≥40°) for a set of bare soils under controlled surfaces roughness, especially for dry sandy soils with high quartz content, with emissivity differences of 14% relative to nadir values. However, there are few studies dealing with the anisotropy of LSE observed from sensors onboard orbiting satellites. For instance, Petitcolin et al. (2002) showed a decrease of up to 3% in bare soil emissivity in Advanced Very High Resolution Radiometer (AVHRR) channels 4 (10.3 - 11.3 μm) and 5 (11.5 - 12.5 μm) using the Temperature Independent Spectral Indices (TISIE) concept (Becker and Li, 1990), and Ren et al. (2011) found a minimal variation of LSE for MODIS band 29 with the zenith angle (<0.005) for barren surfaces when analyzing the MOD11B1 product (Wan, 2007) at 5x5 km^2 resolution.

The objective of the present study is to analyze the anisotropy effects on LSE of bare soils as retrieved from the new MOD21 algorithm which provides 1 km resolution LSTs and LSEs in MODIS bands 29 (8.55 μm), 31 (11 μm) and 32 (12 μm) (Hulley et al., 2012a). The recently proposed MOD21 product is an adaptation of the ASTER TES algorithm (Gillespie et al., 1998) to the MODIS sensor. MODIS TIR at-sensor radiances are atmospherically corrected applying the Water Vapor Scaling (WVS) method (Tonooka 2005) to coincident MOD07 profiles in order to minimize atmospheric correction errors. Since the MOD21 product was not available for this study, we implemented the MOD21 algorithm following the Algorithm Theoretical Basis Document (Hulley et al. 2012a) to simulate the MOD21 product.

The study was carried out over two very homogeneous desert areas: the White Sands (WS) National Monument and the Great Sands (GS) National Park. Arid regions were selected because they are pseudo-invariant dune sites and present the most pronounced decrease of LSE with viewing angle in the TIR region (García-Santos et al., 2012), especially in the

Reststrahlen band from 8 to 9 μm (MODIS band 29). WS is composed by gypsum, which shows a notable Reststrahlen feature as observed from laboratory measurements (Baldridge et al., 2009). GS is composed mainly of quartz (Madole et al., 2008), which is the most important component in many sandy deserts and also shows the Reststrahlen effect. Desert surfaces have also been recognized as optimal targets for long-term validation and calibration of thermal infrared data (de Vries et al., 2007).

The two sites chosen in this study were also selected by Hulley et al. (2009) to validate ASTER LSE retrievals. According to Hulley et al. (2009), sand dunes of WS are displaced around 10 m per year in the North-East direction (McKee, 1966), changing consequently the landscape of the region over a long time period, which implied a temporal variation of ASTER band 11 (8.6 μm) emissivity of 3.1 %, based on 11 ASTER scenes over WS from 2000 to 2008. However, French et al. (2008) found a temporal emissivity variation lower than 0.3% per year at WS analyzing 9 ASTER scenes from 2001 to 2003. The spatial emissivity variation of a 1 x 1 km^2 target site (averaged value of 10×10 ASTER pixels) was 1.2 % for the total 11 observations (Hulley et al., 2009). Regarding GS, a temporal variation of 1.7 % in emissivity for ASTER band 11 was found analyzing 6 ASTER scenes from 2000 to 2008. A spatial emissivity variation of 0.9 % was observed for the whole observations (Hulley et al., 2009).

It is worth to note that LST&E retrievals from a preliminary MOD21 product were validated in 16 different type cover sites, including water, forest, shrublands and barren places (Hulley et al., 2012a). LST results in pseudo-invariant dune sites showed an average bias of +0.2 K and root-mean-square-error (RMSE) of ±1.6 K when using the R-based method (Coll et al., 2009; Wan and Li, 2008). LSE results showed an average bias of +0.0005, and RMSE of ±0.006 between laboratory measurements and MOD21 LSE in band 31 (11 μm) for the same pseudo-invariant dune sites (see Table 10 in Hulley et al. 2012a).

The paper proceeds as follows. Section 2 describes the two test sites selected to carry out the study. Section 3 explains briefly the main notions of the MOD21 algorithm. The data used and the application of the MOD21 algorithm is explained in Section 4. The main results regarding LSE anisotropy over the two sites are shown and discussed in section 5, including a comparison with field data. Finally, conclusions are outlined in section 6.

2. STUDY AREAS

The White Sands (WS) National Monument (Fig. 1a), located in Tularosa Valley (South-central New Mexico, USA) is a dune system desert at 1216 m above sea level, with an area of 704 km^2 and a maximum dune height of 10 m. The grain size is considered fine sand and the major mineralogy component is gypsum according to X-ray diffraction measurements (Hulley et al., 2009).

The second site selected was the Great Sands (GS) National Park (Fig. 1b), located in the San Luis Valley (Colorado, USA). GS covers an area of 104 km^2 at 2560 m above sea level and the maximum dune height (230 m) is quite larger than WS dunes. GS is also a sand dune system desert, created from quartz and volcanic fragments derived from Santa Fe and Alamosa formations. The major mineral is quartz, with minor traces of potassium and feldspar. The grain size of the sand is medium to coarse according to the X-ray diffraction measurements (Hulley et al., 2009).

For the present study, coordinates of the WS sampling are 32.8038° N, 106.2742° W (blue point in Fig. 1a) and for GS are 37.7589° N, 105.5514° W (blue point in Fig. 1b). These areas are coincident with the regions selected by Hulley et al. (2009) to collect soil samples for laboratory emissivity and soil composition measurements.

INSERT FIGURE 1

According to Mira et al. (2010) and García-Santos et al. (2014), WS is 100% sand, which is composed of gypsum in 99% and quartz in 1%. On the other hand, according to the *Soil Survey webpage tool* (http://websoilsurvey.sc.egov.usda.gov/App/HomePage.htm, last access September 2014), GS is composed of sand in 98%, silt in 1.5 % and clay in 0.5 %. GS is composed of quartz in 28% and volcanic rock in 52% (Madole et al., 2008).

3. MODIS AND ANCILLARY DATA USED TO SIMULATE MOD21 PRODUCT

The MOD21 product was not available at the time of the present study. For that reason, it was simulated following the algorithm theoretical basis document (Hulley et al., 2012a) as described in section 4. In this way, we were able to retrieve LST&E at 1 km^2 spatial resolution twice a day, using the MODIS-Terra products MOD021KM and MOD07.

The MOD21 algorithm is applied to the TOA MODIS radiances from bands 29, 31 and 32, included in the MOD021KM product (MODIS Characterization Support Team, 2012). The Level 1B collection contains calibrated and geolocated radiances in W m^{-2} μm^{-1} sr^{-1} for all 36 MODIS spectral bands at 1 km resolution. Radiances were extracted from the *EV_1KM_Emissive Science Data Sets (SDS)* for TIR emissive spectral regions, included in the HDF format MODIS product.

Atmospheric profiles are provided by the MOD07 product (Seemann et al., 2006). Theses profiles are used for the atmospheric correction of the geo-located TOA radiances. The Level 2 MOD07 product consists of several atmospheric parameters produced day and night at 5 km × 5 km resolution. Air temperature and moisture profiles are provided at 20 vertical levels. Uncertainties attributed to the atmospheric parameters provided by MOD07 product are: ±1.9 K for air temperature, ±4 K for the dew point, and ±10 % for relative humidity (Seemann et al., 2006).

In the MOD21 simulated product, it is necessary to discriminate between bare soils and graybody surfaces (water and vegetation). This was done from normalized difference vegetation index (NDVI) data from the monthly MOD13A3 product at 1 km^2 spatial resolution (Solano et al., 2010). According to Hulley et al. (2012a), we considered pixels with 0<NDVI≤0.3 as bare soil, and pixels with NDVI<0 (water) and NDVI>0.3 (vegetation) as graybodies.

A set of MODIS images acquired during 4 years (2010 to 2013) over both selected deserts was considered for the application of the MOD21 algorithm. The total number of MODIS scenes for each study area was 6034 MOD021KM and MOD07 product images (3017 each) and 48 scenes of the MOD13A3 product.

4. MOD21 ALGORITHM THEORETICAL BASIS

In this section, the main theoretical basis of the forthcoming MOD21 product is explained describing the atmospheric correction performed by the Water Vapor Scaling (WVS) method (Tonooka, 2005) and the modified TES method adapted to the three MODIS thermal bands 29 (8.55 µm), 31 (11 µm) and 32 (12 µm). Originally, the WVS and TES methods were developed for the five TIR bands of the ASTER instrument.

4.1 Water Vapor Scaling (WVS) Method

The top-of-atmosphere (TOA) radiances ($L_{sen,i}$) measured by the MODIS sensor must be previously corrected for atmospheric effects using the radiative transfer equation, in order to obtain the at-surface radiance ($L_{sur,i}$) in band *i* (*i*=29, 31 and 32) as:

$$L_{sur,i} = \frac{L_{sen,i} - L_i^{\uparrow}}{\tau_i} \quad (1)$$

where $L_i^{\uparrow}$ and τ_i are the atmospheric path radiance and transmittance, respectively. View angle is not included in Eq. (1) for simplicity.

The atmospheric terms in Eq. (1) are calculated using the 5x5 km^2 atmospheric profiles provided by the MOD07 product (Seemann et al., 2006), which are introduced in the MODTRAN radiative transfer code (version 5.2.1, Berk et al., 2006). These terms are retrieved from outputs of a MATLAB code provided by Griffith (2012), which runs the atmospheric profiles into the MODTRAN iteratively. However, since TES is a very sensitive method to atmospheric correction uncertainties, especially over graybodies such as vegetation, snow or water (Coll et al., 2007; Hulley & Hook 2009b), the atmospheric variables need to be previously refined by applying the WVS method (Tonooka, 2005) in order to minimize error on LST&E.

The first step of the WVS method is to calculate the at-surface brightness temperature from the at-sensor brightness temperature measured at the three selected MODIS bands, based on a multichannel algorithm dependent on the total column water (*TCW*, in cm):

$$T_{g,i} = \alpha_{i,0} + \sum_{k=1}^{n} \alpha_{i,k} T_k \tag{2}$$

$$\alpha_{i,k} = p_{i,k} + q_{i,k} TCW + r_{i,k} TCW^2 \tag{3}$$

where i is band number, n number of bands, $\alpha_{i,k}$ are band-dependent coefficients calculated from p, q and r which are regression coefficients for each band, T_k is the brightness surface temperature for band k (in K) and $T_{g,i}$ is the brightness surface temperature for band i.

The WVS method enhances the accuracy of water vapor atmospheric profiles on a pixel-by-pixel and band-by-band basis by computing a water vapor scaling factor γ, which is used to recalculate the atmospheric transmittance (τ_i) and atmospheric path radiance ($L_i^{\uparrow}$), and it is defined by:

$$\gamma^{\alpha_i} = \frac{\ln\left(\frac{\tau_i(\theta,\gamma_2)^{\gamma_1^{\alpha_i}}}{\tau_i(\theta,\gamma_1)^{\gamma_2^{\alpha_i}}} \cdot \left(\frac{B_i(T_{g,i}) - \frac{L_i^{\uparrow}(\theta,\gamma_1)}{1-\tau_i(\theta,\gamma_1)}}{L_i - \frac{L_i^{\uparrow}(\theta,\gamma_1)}{1-\tau_i(\theta,\gamma_1)}}\right)^{\gamma_1^{\alpha_i} - \gamma_2^{\alpha_i}}\right)}{\ln\left(\frac{\tau_i(\theta,\gamma_2)}{\tau_i(\theta,\gamma_1)}\right)} \tag{4}$$

where α_i is a band model parameter, γ_1=1 and γ_2=0.7 are typical values (Tonooka, 2005), $\tau_i(\theta, \gamma_{1,2})$ are transmittances and $L_i^{\uparrow}(\theta, \gamma_{1,2})$ are path radiances calculated with water vapor profile scaled by $\gamma_{1,2}$.

The scaling factor (γ) is firstly calculated for graybody pixels. For non-graybody pixels, γ is calculated after horizontally interpolating and smoothing the scaling factor from all the graybody surfaces adjacent to the remaining pixels in an *effective radius* of 50 km (Hulley et al., 2012a). Once γ has been calculated, or interpolated and smoothed, the atmospheric parameters τ_i and $L_i^{\uparrow}$ are obtained as

$$\tau_i(\theta, \gamma) = \tau_i(\theta, \gamma_1)^{\frac{\gamma^{\alpha_i} - \gamma_2^{\alpha_i}}{\gamma_1^{\alpha_i} - \gamma_2^{\alpha_i}}} \cdot \tau_i(\theta, \gamma_2)^{\frac{\gamma_1^{\alpha_i} - \gamma^{\alpha_i}}{\gamma_1^{\alpha_i} - \gamma_2^{\alpha_i}}} \quad (5)$$

$$L_i^{\uparrow}(\theta, \gamma) = L_i^{\uparrow}(\theta, \gamma_1) \cdot \frac{1 - \tau_i(\theta, \gamma)}{1 - \tau_i(\theta, \gamma_1)} \quad (6)$$

The hemispherical downwelling sky radiance ($L^{\downarrow}{}_{hem,i}$), which is required for the application of the TES method, can be obtained from a non-linear equation, as a function of the path radiance at nadir view as follows:

$$L_{hem,i}^{\downarrow}(\gamma) = a_i + b_i \cdot L_i^{\uparrow}(0^{\circ}, \gamma) + c_i \cdot L_i^{\uparrow}(0^{\circ}, \gamma)^2 \quad (7)$$

$$L_i^{\uparrow}(0^{\circ}, \gamma) = L_i^{\uparrow}(\theta, \gamma) \cdot \frac{1 - \tau_i(\theta, \gamma)^{\cos\theta}}{1 - \tau_i(\theta, \gamma)} \quad (8)$$

Values of coefficients in equations (2)-(6) as well as further details about the WVS method can be found in chapter 5 of Hulley et al. (2012a).

4.2 Temperature and Emissivity Separation (TES) Method

Eq. (1) is composed by the radiance emitted by the surface and the reflected hemispherical downwelling radiance ($L^{\downarrow}{}_{hem}$, obtained from the WVS as described above):

$$L_{sur,i} = \varepsilon_i B_i(T) - [1 - \varepsilon_i] L^{\downarrow}{}_{hem,i} \quad (9)$$

where ε_i is the surface emissivity, and $B_i(T)$ is the Planck function for blackbody spectral radiance at temperature *T*.

The TES method starts with the Normalized Emissivity Method (NEM) module, which requires $L_{sur,i}$ and $L^{\downarrow}{}_{hem,i}$, together with an initial ε_i value (ε_i=0.98 in this study) to calculate B_i(T) from eq. (9). The next step is inverting the Planck function and retrieving a temperature in the three MODIS bands 29, 31 and 32. The maximum of these three temperatures is selected (T_{NEM}). Now this T_{NEM} is used to calculate $B_i(T_{NEM})$, and three emissivities (one per spectral band) are retrieved from eq. (9). With these emissivities, $L_{sur,i}$ is recalculated using Eq. (9). This process is repeated until convergence; that is when the change in $L_{sur,i}$ between iterations is less than a threshold;, equivalent to the sensor noise-equivalent differential temperature (±0.05 K for MODIS).

The RATIO module uses the NEM emissivities to calculate the beta (β_i) spectrum as the ratio of each band emissivity to the average emissivity value ($\bar{\varepsilon}$), as follows:

$$\beta_i = \frac{\varepsilon_i}{\bar{\varepsilon}} \tag{10}$$

The Maximum-Minimum Difference (MMD) is obtained from the β_i spectrum as MMD=max(β_i)-min(β_i). Finally the MMD value is introduced in an empirical relationship to calculate the minimum emissivity as:

$$\varepsilon_{min} = \alpha_1 - \alpha_2 MMD^{\alpha_3} \tag{11}$$

where α_1=0.985, α_2=0.7503 and α_3=0.8321 are coefficients given in Hulley et al. (2012a).

From the minimum emissivity of Eq. (11) and the β_i spectrum, the absolute emissivity is obtained through

$$\varepsilon_i = \frac{\varepsilon_{min}\,\beta_i}{\min(\beta_i)} \tag{12}$$

Finally the LST is calculated using the maximum value of the TES emissivities in Eq. (9) for the band where the maximum emissivity occurs.

Hulley et al. (2012b) derived a quadratic polynomial that predicts the uncertainty in MOD21 LST&E retrievals depending on the total column water and zenith angle (θ). Coefficients for the LST and emissivity uncertainty polynomials are dependent on surface type (gray bodies, transition zones or bare surfaces) (Hulley, personal communication). Further details about the MOD21 product can be found in the MOD21 ATBD (Hulley et al., 2012a).

Two limitations were imposed to the MODIS data in order to reduce the uncertainty in the MOD21 results. First, only scenes with a TCW lower or equal than 1.5 cm were used. The *TCW* limitation was imposed because, for viewing zenith angle of 53.7° and *TCW* values larger than 1.5 cm, MOD21 results show LST predicted errors larger than ±1 K, and band 29 LSE errors of ±0.03 for rocks, soils and sand surfaces (Hulley et al., 2012a). Therefore, limiting the study to drier atmospheres reduced the uncertainty on LSE retrievals for our selected soils.

The second limitation was that only MODIS scenes were considered with at least 70% of cloud-free pixels inside the 50 km radius circle centered in the selected coordinates. The reason is to get enough cloud-free, graybody pixels in the 50 km radius circle and therefore to improve the interpolation and smoothing of the WVS γ factors for the non-graybody pixels. Figure 2 shows an example of the graybody pixels included in the 50 km radius for the two sites. Both scenes were obtained from monthly NDVI data of the MOD13A3 product for April, 2010. All pixels with NDVI<0 (water) or NDVI>0.3 (vegetation) were considered as graybody, whereas the remaining pixels were considered as bare soil. The mean number of pixels included inside the circle is around 7400, for which around 900 pixels were considered as graybody (12%) for WS and 4200 pixels (57%) for GS. As observed in Fig. 2, because of the lower number of graybody pixels, the interpolation and smoothing of the γ factors is more difficult for WS than for GS. However, we consider that they are enough for the application of the WVS method.

INSERT FIGURE 2

After applying the TCW and cloud limitations, 686 scenes (335 daytime and 351 nighttime) were selected for WS, and 689 scenes (366 daytime and 323 nighttime) were selected for GS. LSEs were obtained using the MOD21 simulated product for MODIS bands 29, 31 and 32 at different viewing angles. While the selected data covered adequately the zenith viewing angle range of MODIS (0°-65°) over the two sites, the azimuthal viewing angles were limited to a relatively narrow range. For nighttime overpasses, the azimuthal angles (from North) were between -94° and -105° for WS, and between -92° and -103° for GS (MODIS crossing the West side of the sites); and between 74°- 83° for WS, and 73°- 92° for GS (MODIS crossing the East side of the sites). For daytime overpasses, the azimuthal angles are between -75° and -117° for WS, and -72° and -84° for GS (West side overpass); and between 80° - 102° for WS, and 94° - 108° for GS (East side overpass). In summary, we divided azimuthal observations in two different orientations, West or East, considering zenithal observation angles negative for West azimuths and positive for East azimuths.

The procedure to obtain a LSE value for a specific zenith angle (θ) was as follows. For each MODIS scene and site only pixels no more than 1 km away from the site coordinates were considered. For such pixels (usually 4), a spatially-averaged LSE value wascalculated. The spatially-averaged LSE values were grouped by zenith viewing angle into 1° wide intervals from -65° to 65°. According to Schneider et al. (2012), robust statistics are recommended because they minimize the influence of possible outliers and can be considered more consistent than standard statistics. For that reason, we calculated the median (Me) and the robust standard deviation (RSD) to all the zenithal-grouped LSE values to obtain the emissivity value and the corresponding uncertainty, respectively, for a specific zenith angle interval. The RSD is defined as:

$$\mathrm{RSD} = \mathrm{Me}(|\varepsilon_i - \mathrm{Me}(\varepsilon_i)|) \cdot 1.4826 \qquad (13)$$

5. RESULTS AND DISCUSSION

Figure 3 shows maps of LST&E MOD21 simulated product at MODIS scale (1 km^2) for the two studied regions. The desert area is outlined and the sampling site is marked in both cases. From these data, the average values ± standard deviation of the emissivity and LST of the four pixels within the blue square were 0.783 ±0.010 (band 29), 0.971 ±0.001 (band 31), 0.965 ±0.001 (band 32) and 17.2 ±0.3 K (LST) for WS. For GS, the LST&E values were 0.896 ±0.004 (band 29), 0.949 ±0.002 (band 31), 0.969 ±0.001 (band 32) and 36.4 ±0.4 K. These examples show the spatial homogeneity in LST&E of the selected sites.

The LSE maps for band 29 show the lowest values in areas within the desert sites, as a consequence of the quartz and gypsum Reststrahlen feature at 8-9 µm. LSE for bands 31 and 32 shows close and uniform values along the WS desert extension. In GS, LSE for band 31 is significantly lower than for band 32, both values being also uniform over the desert area.

INSERT FIGURE 3

5.1 Analysis of uncertainties

Maximum, minimum and average RSD values for both WS and GS sites are shown in Table 1 for the three MODIS thermal bands 29 (8.4 - 8.7 µm), 31 (10.78 - 11.28 µm) and 32 (11.77 - 12.27 µm). Uncertainties in table 1 are both for nighttime and daytime. Uncertainties predicted from Hulley et al. (2012b) over WS and GS ranged from ±0.016 to ±0.023 for band 29, and between ±0.012 and ±0.014 for bands 31 and 32 (for the two selected sites and both nighttime and daytime). Therefore, our uncertainties were within the uncertainties predicted by Hulley et al. (2012b) for all viewing angles for bands 31 and 32, but were slightly higher for band 29.

INSERT TABLE 1

5.2 Analysis of nadir emissivities

a) Comparison with laboratory data

Figure 4 shows MOD21 simulated LSE retrievals at near-nadir (2°-16°) at both sites for day (17H-19H UTC, 10H-13H Local Time) and nighttime (4H-6H UTC, 21H-24H Local Time) MODIS overpasses. For both sites, MOD21 LSE is compared with emissivity values obtained from laboratory spectral measurements for samples collected from the study areas (Glynn Hulley, personal communication), which were weighted for MODIS-Terra bands 29, 31 and 32 using the appropriate filter functions.

INSERT FIGURE 4

Table 2 shows the difference between the above mentioned measured emissivity and that calculated from MOD21 algorithm, both day ($\Delta\varepsilon_d$) and night ($\Delta\varepsilon_n$) in the two studied areas. In both sites results showed that MOD21 LSEs overestimated band-averaged laboratory values, independently of the time overpass and sensor spectral band. LSE values for bands 31 and 32 (for both sites and sensor overpass) can be considered in good agreement with laboratory data, because they were within the predicted uncertainty (±0.001 to ±0.012).

However, MOD21 LSE for band 29 showed the highest discrepancies between day and nighttime overpasses. So for WS site daytime LSE overestimated laboratory emissivity data, but this overestimation is explained in terms of uncertainty (±0.014 to ±0.022). This was not the case of nighttime LSE overestimation for band 29. Similarly to WS, overestimation of MOD21 LSE for band 29 in GS was justified in terms of the associated uncertainty (±0.019 to ±0.030) for the daytime sensor overpass, but not for the nighttime overpass.

It is worth to note that despite the poor interpolation and smoothing for the application of the WVS method in the WS case, the uncertainty associated the LSE retrieval was lower than or of the same order as for the GS site (Figure 4), where the interpolation and smoothing process was theoretically better, since there were more graybody pixels surrounding the desert.

INSERT TABLE 2

b) Soil moisture effect observed between day and nighttime

Figure 4 shows a bias in band 29 LSE depending on the sensor time overpass, so for nighttime, band 29 LSE presented a value +0.027 larger than for the daytime overpass at the WS site. For the same site, the bias between night and daytime LSE for bands 31 and 32 was 0.004 and 0.001, respectively. For GS (Figure 4b) nighttime LSEs showed an average value 0.010, 0.002 and 0.003 larger than the corresponding daytime value for bands 29, 31 and 32, respectively. According to Hulley et al. (2012a), daily variation in surface soil moisture is the main factor potentially affecting the temporal stability of dune sites, since emissivity increases with soil moisture (Mira et al., 2010; Hulley et al., 2010; Sánchez et al., 2011; García-Santos et al., 2014). The positive bias between nighttime and daytime emissivities obtained using satellite estimates over desert areas has been observed in previous studies. Li et al. (2012) used LSE retrievals from the geostationary SEVIRI sensor over the whole Sahara desert to show night-day differences up to 0.03 for the 8.7 µm channel. LSEs for channels 10.8 µm and 12 µm showed no significant diurnal variation. Similar results were obtained by Masiello et al. (2014) with Infrared Atmospheric Sounding Interferometer (IASI) data over the Sahara desert and by Rozenstein et al. (2015) using SEVIRI data and field spectral measurements over the Sinai and Negev deserts. The night-day LSE variations observed in our two selected sites (Figure 4) were in good agreement with those results.

Since rainfall events are rare in desert areas and cannot explain the systematic night-day emissivity bias observed, we checked the possibility of dew formation over the WS site using hourly meteorological data from the Holloman weather station (http://www.wunderground.com/weather-forecast/US/NM/Holloman_Air_Force_Base.html), located 10 km away from the WS site. Dew is only formed when the air temperature is equal or lower than the dew point temperature, which only occurred in 20 cases out of the 1461 days analyzed in 2010-2013. Using data for the same weather station, we found that rainfall occurred only for 84 out of 1460 days. Therefore, nighttime dew formation and rainfall cannot be the cause of the night-day LSE differences for the majority of the scenes. A similar conclusion was drawn by Li et al. (2012), Masiello et al. (2014), and Rozenstein et al. (2015), who found very unlikely the formation of dew in arid, desert areas. They attributed the nighttime increase of the soil moisture to direct water vapor adsorption by the soil, which happens when the relative humidity of the soil pores is lower than the relative humidity of the air, and the air temperature is higher than the dew point temperature (Agam & Berliner, 2006). Water vapor adsorption has a diurnal cycle, decreasing during the day (beginning 1-2 hours before the sunrise) and increasing at night (beginning 2-4 h before the sunset). Experimental measurements in a dry desert area showed that water vapor adsorption can increase the soil moisture in the uppermost 1-cm soil layer by 2% (Agam & Berliner, 2006). Therefore, we consider that the night-day LST differences were likely due to variations in soil moisture caused by water vapor adsorption. The different magnitude of the effect in WS and GS may be due to the different nature of the soils, and the higher altitude of the GS site where less atmospheric water vapor is available. However, further studies would be required including the analysis of LSE retrieval for other desert sites in combination with meteorological data, or dedicated field campaigns with meteorological, soil moisture and LSE measurements, which are out of the scope of the present paper.

5.3 Angular variation of emissivities

INSERT FIGURE 5

Figure 5 shows the MOD21 LSE variation with zenith angle for the three bands and the two sites selected. It shows that LSE for the three MODIS thermal bands was almost completely independent of the azimuthal orientation (West and East overpasses, see section 4). Table 3 shows the absolute value of the average differences between West and East LSEs for the same zenithal angle at both studied sites and for the two different MODIS time overpasses. Results showed that LSE could be considered independent of the azimuthal observation since the possible variation is lower than the corresponding uncertainty associated to all spectral bands and sensor overpass times (see Table 1).

INSERT TABLE 3

Regarding the zenithal dependence, LSE in MODIS bands 31 and 32 were nearly constant and independent of viewing angle and sensor overpass time. Table 4 shows the average LSE value and RSD for all zenithal angles of Figure 5 for MODIS bands 31 and 32 and both sites. Maximum difference between nadir and off-nadir LSE ($\Delta\varepsilon_\theta$) were also included. As observed in Table 2, possible angular variations of LSE in MODIS bands 31 and 32 over arid regions were smaller than the uncertainty associated to retrieved LSE values.

INSERT TABLE 4

However, results were different for MODIS band 29, in which the LSE dependence on viewing angle was significant both at night and day. Band 29 LSE retrieved from MOD21 decreased with θ independently of the azimuthal orientation and the passing time of the sensor. LSE reached a maximum decrease, between values at $\theta \leq 15°$ and values at $\theta \geq 50°$, of 0.030 (nighttime) and 0.038 (day time) for WS, and 0.033 (nighttime) and 0.021 (daytime) for GS. Such decreases cannot be explained in terms of uncertainties and only the anisotropy associated to sandy soil emissivity (Labed & Stoll, 1991; Cuenca & Sobrino, 2004; García-Santos et al., 2012) can be the reason.

5.4 Validation of an emissivity anisotropy model

García-Santos et al. (2014) analyzed the variation of LSE with viewing angle (θ) and soil moisture (SM) using laboratory measurements taken with a multispectral thermal radiometer CIMEL Electronique CE-312 (Brogniez et al. 2003) at five different spectral bands within 8-14 µm. García-Santos et al. (2014) also derived a polynomial expression of the relative-to-nadir LSE as a function of θ and SM according to:

$$\varepsilon_{ri}(SM,\theta) = a_i + b_i\, SM + c_i\,\theta + d_i SM^2 + e_i\, SM\,\theta + f_i\theta^2 \tag{14}$$

where ε_r is the relative-to-nadir emissivity, *i* is the spectral band, and coefficients *a, b, c, d, e* and *f* are polynomials dependent on percentages of quartz (Q) and clay (C) content of the considered soil sample, following the expression:

$$a_i(C,Q) = p_0 + p_1 C + p_2 Q + p_3 C^2 + p_4\, C\, Q + p_5 Q^2 \tag{15}$$

Equation (15) also holds for coefficients *b* to *f*. Values and uncertainties of the regression coefficients *a*-*f* and p_0-p_5 are tabulated in Garcia-Santos et al. (2014). SM data can be obtained twice a day and at spatial resolution of 40 km^2 using the measurements of the SMOS instrument (Soil Moisture and Ocean Salinity, Mecklenburg et al.,2012) with an uncertainty of ±0.3 m^3/m^3 (units of volumetric SM). The zenithal angle is well established by the MODIS sensor. Finally, percentages of C and Q can be obtained from different techniques described in Singh and Kathpalia (2007) and Ninomiya and Fu (2001), respectively, with an uncertainty between 0.7 % and 0.18 %. We made a simple sensitivity analysis of the emissivity model to the uncertainties associated to the input data SM, C and Q. We calculated the difference between the LSE obtained through eqs. (14) and (15) considering the prescribed values of SM=0, C and Q (given in section 2 for both sites) and that obtained after increasing/decreasing these values by their corresponding uncertainties given above. Results showed an average LSE uncertainty of ± 0.009 for both sites.

The LSE anisotropy for MODIS band 29 observed in this study for the WS and GS deserts was compared to that predicted by Eqs. (14) and (15). Only results for daytime MODIS overpasses were used to assure dry soil conditions considering SM zero in Eq. (14), since analyzing hourly data from a weather station near to WS site no rainfall events were found coincident or close to MODIS daytime overpasses. Moreover, no measured values of SM were available and SM data from SMOS was not considered since spatial resolution of SMOS (40 km^2) is much large than MODIS (1 km^2) and more important, there is about 3:30 h hour delay between MODIS and SMOS overpasses (SMOS daytime pass at 12:30-13:30 UTC and nighttime pass at 1:30-2:30 UTC) in both areas. According to Hulley et al (2012a) the lifetime of soil moisture at the dune sites is most likely small due to large sensible heat fluxes, high evaporation rates, in addition to rapid infiltration. It is worth to note that WS was one of the 12 bare soil samples analyzed in García-Santos et al. (2014), so values of LSE at specific zenith angles were measured in laboratory conditions, and they can be used to validate MOD21 LSE values in WS.

Figure 6 shows MODIS band 29 LSEs for WS and GS, comparing MOD21 retrievals averaged for all the East and West orientations (since there was not azimuthal dependence on azimuthal observation according to Table 3) with the model-predicted LSE values, calculated by multiplying the most close-to-nadir MOD21 emissivity value (0.809 for WS and 0.909 for GS) by the values given by Eq. (14). WS emissivity values measured in García-Santos et al. (2014) for channel 5 (8.4-8.9 µm) of the CE-312 instrument in the zenith angle range 10°-60° (with a 10° interval), were also included in Figure 6.

INSERT FIGURE 6.

Results from Figure 6 showed that LSE anisotropy predicted by Eqs. (14) and (15) (García-Santos et al.,2014) agreed with MOD21 retrievals, with an average bias between predicted and retrieved LSE of -0.003 for WS and +0.005 for GS and RMSE of ±0.009 and ±0.010 for WS and GS, respectively. Therefore Eqs. (14) and (15) are applicable to satellite data at the MODIS spatial resolution, at least for the WS and GS bare soils.

6. CONCLUSIONS

LST&E MOD21 will be part of the future MODIS collection 6 products. The TES algorithm was implemented together with the WVS method for use with the three MODIS thermal bands 29, 31 and 32. MOD21 data were simulated over the WS and GS deserts to analyze the anisotropy of LSE. Results showed that LSE did not depend on the zenithal viewing angle for bands 31 and 32 (11 and 12 µm). However, LSE decreased significantly with zenith angle for band 29 (8.55 µm), reaching differences up to 0.038 from nadir values. LSE for band 29 showed a bias depending on the sensor time overpass, so for nighttime passes, band 29 LSE presented a value +0.027 (WS) and +0.008 (GS) greater than LSE for the respective daytime overpass, independently of the viewing angle. An explanation could be the increase of the soil moisture due to water vapor adsorption, and therefore the corresponding increase of LSE.

Nadir LSE values and observed zenithal variations retrieved from MOD21 measurements were compared with predicted values from an empirical model based on angular LSE measurements taken under field conditions. Results showed the validity of the proposed parameterization and its applicability to satellite data for a MODIS pixel resolution (1 km^2), since MOD21 LSE retrievals agreed with laboratory measurements.

The good agreement between laboratory LSE measurements and MOD21 LSE retrievals at different zenithal angles contributes to the validation of the forthcoming MOD21 LST&E product.

Acknowledgement: Authors are very thankful to Dr. Glynn Hulley for assisting us with the implementation of the MOD21 algorithm, as well for as providing us with the emissivity spectra of WS and GS samples. We thank the anonymous reviewers who helped to improve the manuscript. This study was supported by the Vali+D postdoctoral program (exp. APOSTD/2015/033) of the Conselleria d'Educació, Cultura I Esport, Generalitat Valenciana and Spanish Ministry of Economy and Competitiveness, through projects CGL2013-46862-C2-1-P and CGL2011-30433-C02-02, and through the "Ramón y Cajal" Research Contract of Dr. Niclòs .

We also want to thank the Government of Generalitat Valenciana to support this study through the project PROMETEOII/2014/086.

REFERENCES

Agam, N., and P. R. Berliner (2006), Dew formation and water vapor adsorption in semi-arid environments: A review, *Journal of Arid Environments*, 65, 572–590, doi:10.1016/j.jaridenv.2005.09.004.

Baldridge, A.M., Hook, S. J., Grove, C. I., & Rivera, G. (2009). The ASTER Spectral Library Version 2.0. *Remote Sensing of Environment*, 114, 711–715.

Becker, F. & Li, Z.L. (1990). Temperature Independent Spectral Indices in thermal infrared bands. Remote Sensing of Environment, 32, 17-33.

Berk, A., G.P. Anderson, P.K. Acharya, L.S. Bernstein, L. Muratov, J. Lee, M. Fox, S.M. Adler-Golden, J.H. Chetwynd, M.L. Hoke, R.B Lockwood, J.A. Gardner, T.W. Cooley, C.C. Borel, P.E. Lewis and E.P. Shettle (2006). MODTRAN5: 2006 Update, *Proc. SPIE*, 6233, 62331F.

Brogniez, G., Pietras, C., Legrand, M., Dubuisson, P., & Haeffelin, M. (2003). A high-accuracy multiwavelength radiometer for in situ measurements in the thermal infrared. Part II: Behavior in field experiments. *Journal of Atmospheric and Oceanic Technology*,20, 1023-1033.

Coll, C., Caselles, V., Valor, E., Niclos, R., Sanchez, J.M., Galve, J.M., & Mira, M. (2007). Temperature and emissivity separation from ASTER data for low spectral contrast surfaces. *Remote Sensing of Environment*, 110, 162-175.

Coll, C., Wan, Z.M., & Galve, J.M. (2009). Temperature-based and radiance-based validations of the V5 MODIS land surface temperature product. *Journal of Geophysical Research-Atmospheres*, 114.

Cuenca, J., & Sobrino, J.A. (2004). Experimental measurements for studying angular and spectral variation of thermal infrared emissivity. *Applied Optics*, 43, 4598-4602.

Dash, P., Gottsche, F. M., Olesen, F. S., & Fischer, H. (2002). Land surface temperature and emissivity estimation from passive sensor data: theory and practice-current trends. *International Journal of Remote Sensing*, 23, 2563–2594.

de Vries, C., Danaher, T., Denham, R., Scarth, P., & Phinn, S. (2007). An operational radiometric calibration procedure for the Landsat sensors based on pseudo-invariant target sites. *Remote Sensing of Environment*, 107, 414-429.

Freitas, S.C., Trigo, I.F., Bioucas-Dias, J.M., & Gottsche, F. M. (2010). Quantifying the Uncertainty of Land Surface Temperature Retrievals From SEVIRI/Meteosat. *IEEE Transactions on Geoscience and Remote Sensing*, 48, 523-534.

French, A. N., Schmugge, T. J., Ritchie, J. C., Hsu, A., Jacob, F., & Ogawa, K. (2008). Detecting land cover change at the Jornada Experimental Range, New Mexico with ASTER emissivities. *Remote Sensing of Environment*, 112, 1730-1748.

French, A. N., & Inamdar, A. (2010). Land cover characterization for hydrological modelling using thermal infrared emissivities. *International Journal of Remote Sensing*, 31, 3867-3883.

Galve, J.A., Coll, C., Caselles, V., & Valor, E. (2008). An atmospheric radiosounding database for generating land surface temperature algorithms. *IEEE Transactions on Geoscience and Remote Sensing*, 46, 1547-1557.

García-Santos, V., Valor, E., Caselles, V., Burgos, M. A., & Coll, C. (2012). On the angular variation of thermal infrared emissivity of inorganic soils. *Journal of Geophysical Research-Atmospheres*, 117.

Garcia-Santos, V., Valor, E., Caselles, V., Coll, C., & Burgos, M.A. (2014). Effect of Soil Moisture on the Angular Variation of Thermal Infrared Emissivity of Inorganic Soils. *IEEE Geoscience and Remote Sensing Letters*, 11, 1091-1095.

Gillespie, A., Rokugawa, S., Matsunaga, T., Cothern, J.S., Hook, S., & Kahle, A.B. (1998). A temperature and emissivity separation algorithm for Advanced Spaceborne Thermal Emission and Reflection Radiometer (ASTER) images. *IEEE Transactions on Geoscience and Remote Sensing*, 36, 1113-1126.

Griffith, D. (2012). Mod5 – A Matlab Class Wrapper for MODTRAN 5. *DPSS, CSIR (Johannesburg, South Africa)*. https://code.google.com/p/matlab-modtran-5/downloads/list (last access in November 2014).

Guillevic, P. C., Biard, J. C., Hulley, G., Privette, C. J. L., Hook, S. J., Olioso, A., Göttsche, F. M., Radocinski, R., Román, M. O., Yu, Y., & Csiszar I. (2014). Validation of Land Surface Temperature products derived from the Visible Infrared Imaging Radiometer Suite (VIIRS) using ground-based and heritage satellite measurements. *Remote Sensing of Environment*, 154, 19-37.

Hulley, G. C., Hook, S. J., & Baldridge, A. M. (2008). ASTER land surface emissivity database of California and Nevada. *Geophysical Research Letters*, 35, L13401. doi:10.1029/2008GL034507.

Hulley, G.C., & Hook, S.J. (2009a). Intercomparison of Versions 4, 4.1 and 5 of the MODIS Land Surface Temperature and Emissivity Products and Validation with Laboratory Measurements of Sand Samples from the Namib Desert, Namibia. *Remote Sensing of Environment*, 113, 1313-1318.

Hulley, G.C., & Hook, S.J. (2009b). The North American ASTER Land Surface Emissivity Database (NAALSED) Version 2.0. *Remote Sensing of Environment*, 1967-1975.

Hulley, G.C., Hook, S.J., & Baldridge, A.M. (2009). Validation of the North American ASTER Land Surface Emissivity Database (NAALSED) Version 2.0 using Pseudo-Invariant Sand Dune Sites. *Remote Sensing of Environment*, 113, 2224-2233.

Hulley G.C., Hook S.J., & Baldridge A. M. (2010). Investigating the effects of soil moisture on thermal infrared land surface temperature and emissivity using satellite retrievals and laboratory measurements. *Remote Sensing of Environment,* 114, 1480–1493.

Hulley, G.C., Hook, S.J., & Hughes, T. (2012a). Moderate Resolution Imaging Spectroradiometer (MODIS) MOD21 Land Surface Temperature and Emissivity Algorithm Theoretical Basis Document. Jet Propulsion Laboratory publication 12-17, National Aeronautics and Space Administration (NASA).

Hulley, G. C., C. G. Hughes, and S. J. Hook (2012b), Quantifying uncertainties in land surface temperature and emissivity retrievals from ASTER and MODIS thermal infrared data, *Journal of Geophysical Research*, 117, D23113, doi:10.1029/2012JD018506.

Hulley, G., Veraverbeke, S., & Hook, S. (2014).Thermal-based techniques for land cover change detection using a new dynamic MODIS multispectral emissivity product (MOD21), *Remote Sensing of Environment*, 140, 755-765.

Jacob, F., Olioso, A., Gu, X. F., Su, Z., & Seguin, B. (2002). Mapping surface fluxes using airborne visible, near infrared, thermal infrared remote sensing data and a spatialized surface energy balance model. *Agronomie*, 22, 669−680.

King, M. D. (1999), EOS Science Plan: The State of Science in the EOS Program, 397, *NASA*, Washington, D. C.

Labed, J., & Stoll M. P. (1991), Angular variation of land surface spectral emissivity in the thermal infrared: Laboratory investigations on bare soils, *International Journal of Remote Sensing,* 12, 2299-2310.

Lagouarde, J. P., Kerr, Y. H. & Brunet, Y. (1995). An experimental study of angular effects on surface temperature for various plant canopies and bare soils. *Agricultural and Forest Meteorology*, 77, 167–190.

Li, J., Weisz, E., & Zhou, D. K. (2007). Physical retrieval of surface emissivity spectrum from hyperspectral infrared radiances. *Geophysical Research Letters*, 34, L16812.

Li Z., Li J., Li Y., Zhang Y., Schmit TJ., Zhou L., Goldberg, M. D., & Menzel W. P. (2012). Determining diurnal variations of land surface emissivity from geostationary satellites. *Journal of Geophysical Research*, 117, D23302.

Li, Z. L., Tang, B. H., Wu, H., Ren, H., Yan, G., Wan, Z., Trigo, I. F., & Sobrino, J. A. (2013). Satellite-derived land surface temperature: Current status and perspectives. *Remote Sensing of Environment*, 131, 14-37. http://dx.doi.org/10.1016/j.rse.2012.12.008.

Madole, R.F., Romig, J.H., Aleinikoff, J.N., Paco VanSistine, D., & Yacob, E.Y. (2008). On the origin and age of the Great Sand Dunes, Colorado. *Geomorphology*, 99, 99-119.

Masiello G., Serio C., Venafra S., DeFeis I., & Borbas, E. E. (2014). Diurnal variation in Sahara desert sand emissivity during the dry season from IASI observations. *Journal of Geophysical Research*, 119, 1626–1638.

McKee, E. D. (1966). Structures of Dunes at White Sands National Monument, New Mexico (and a comparison with structures of dunes from other selected areas). *Sedimentology*, 7, 1−69.

Mecklenburg, S., Drusch, M., Kerr, Y.H., Font, J., Martin-Neira, M., Delwart, S., Buenadicha, G., Reul, N., Daganzo-Eusebio, E., Oliva, R., & Crapolicchio, R. (2012). ESA's Soil Moisture and Ocean Salinity mission: mission performance and operations. *IEEE Transactions on Geoscience and Remote Sensing*, 50(5), 1354–1366.

Mira, M., Valor, E., Caselles, V., Rubio, E., Coll, C., Galve, J.M., Niclos, R., Sanchez, J.M., & Boluda, R. (2010). Soil Moisture Effect on Thermal Infrared (8–13 µm) Emissivity. *IEEE Transactions on Geoscience and Remote Sensing*, 48, 2251-2260.

MODIS Characterization Support Team (2012). MODIS Level 1B Product User's Guide: For Level 1B Version 6.1.14 (Terra) and Version 6.1.17 (Aqua). *MCST Document # PUB-01-U-0202- REV D MCST Internal Memorandum # M1054*. NASA/Goddard Space Flight Center Greenbelt, MD 20771. Latest release is available on-line at: http://mcst.gsfc.nasa.gov/sites/mcst.gsfc/files/file_attachments/M1054D_PUG_083112_final.pdf.

Mushkin, A., & Gillespie, A.R. (2005). Estimating sub-pixel surface roughness using remotely sensed stereoscopic data. *Remote Sensing of Environment*, 99, 75-83.

Ninomiya, Y. & Fu, B. (2001). Spectral indices for lithologic mapping with ASTER thermal infrared data applying to a part of Beishan Mountains, Gansu, China. Proceedings. *IEEE International Geoscience and Remote Sensing Symposium* 2001, 7, 2988–2990.

Norman, J. M., & Becker F. (1995). Terminology in thermal infrared remote sensing of natural surfaces. *Agricultural and Forest Meteorology.* 77, 153-166.

Petitcolin, F., Nerry, F. & Stoll M.P. (2002). Mapping temperature independent spectral indice of emissivity and directional emissivity in AVHRR channels 4 and 5. *International Journal of Remote Sensing*, 23(17), 3473-3491.

Qin, J. Liang, S., Li, X., & Wang, J. (2008). Development of the Adjoint Model of a Canopy Radiative Transfer Model for Sensitivity Study and Inversion of Leaf Area Index. *IEEE Transactions on Geoscience and Remote Sensing*, 46, 2028-2037.

Ren, H., Yan, G., Chen, L. & Li, Z. (2011). Angular effect of MODIS emissivity products and its application to the split-window algorithm, *ISPRS Journal of Photogrammetry and Remote Sensing*, 66, 498-507.

Rozenstein, O., Agam, N., Serio, C., Masiello, G., Venafra, S., Achal, S., Puckrin, E., & Karnieli, A. (2015). Diurnal emissivity dynamics in bare versus biocrusted sand dunes. *Science of The Total Environment*, 506–507, 422-429.

Sánchez, J. M., Scavone, G., Caselles, V., Valor, E., Copertino, V. A., & Telesca, V. (2008). Monitoring daily evapotranspiration at a regional scale from Landsat-TM and ETM+ data: Application to the Basilicata region. *Journal of Hydrology*, 351, 58-70.

Sanchez J. M., French A. N., Mira M., Hunsaker D. J., Thorp K. R., Valor E., & Caselles V. (2011). Thermal infrared emissivity dependence on soil moisture in field conditions. *IEEE Transactions on Geoscience and Remote Sensing,* 49, 4652–4659.

Schneider, P., Ghent, D., Corlett, G., Prata, F., & Remedios, J. (2012). AATSR validation: LST validation protocol. *Internal publication, UL-NILU-ESA-LST-LVP*, 1, 39 (Available on line at http://lst.nilu.no/Portals/73/Docs/Reports/UL-NILU-ESA-LST-LVP-Issue1-Rev0-1604212.pdf).

Seemann, S. W., Borbas, E. E., Li, J., Menzel, W. P. & Gumley, L. E. (2006). Modis Atmospheric Profile Retrieval Algorithm Theoretical Basis Document. *Cooperative Institute for Meteorological Satellite Studies University of Wisconsin-Madison*. Version 6 October 25, 2006.

Singh, D., & Kathpalia, A. (2007). An efficient modeling with GA approach to retrieve soil texture, moisture and roughness from ERS-2 SAR data. *Progress in Electromagnetic Research*.77, 121–136. doi:10.2528/PIER07071803.

Solano, R., Didan, K., Jacobson, A. & Huete, A. (2010). MODIS Vegetation Index User’s Guide (MOD13 Series). Version 2.00, May 2010 (Collection 5). The University of Arizona.

Tonooka, H. (2005). Accurate atmospheric correction of ASTER thermal infrared imagery using the WVS method. *IEEE Transactions on Geoscience and Remote Sensing*, 43, 2778-2792.

Wan, Z. and Dozier, J. (1996). A generalized split-window algorithm for retrieving land-surface temperature from space. *IEEE Transactions on Geoscience and Remote Sensing*, 34, 892-905.

Wan, Z. (1999). MODIS Land-Surface Temperature Algorithm Theoretical Basis Document (LST ATBD). *ICESS, University of California, Santa Barbara*.

Wan, Z. (2007). Collection-5 MODIS Land Surface Temperature Products Users' Guide. *ICESS, University of California, Santa Barbara,* March, 2007.

Wan, Z., & Li, Z.L. (2008). Radiance-based validation of the V5 MODIS land-surface temperature product. *International Journal of Remote Sensing,* 29 (17–18), 5373–5395.

Wan, Z. (2014). New refinements and validation of the collection-6 MODIS land-surface temperature/emissivity product. *Greenbelt MD, USA: NASA/GSFC*. *Remote Sensing of Environment*, 140, 36-45.

Yu, Y., Tarpley, D., Privette, J.L., Flynn, L.E., Hui Xu, Ming Chen, Vinnikov, K.Y., Sun, D., & Tian, Y. (2012). Validation of GOES-R Satellite Land Surface Temperature Algorithm Using SURFRAD Ground Measurements and Statistical Estimates of Error Properties. *IEEE Transactions on Geoscience and Remote Sensing*, 50, 704-713.

TABLES

Table 1. Maximum, minimum and average RSD values for both studied sites and MODIS overpass time at the three spectral bands 29 (8.4 - 8.7 μm), 31 (10.78 - 11.28 μm) and 32 (11.77 - 12.27 μm).

	White Sands			Great Sands		
	B29	B31	B32	B29	B31	B32
Maximum	±0.03	±0.008	±0.008	±0.03	±0.014	±0.014
Minimum	±0.006	±0.0002	±0.0002	±0.009	±0.0005	±0.0005
Average	±0.015	±0.001	±0.001	±0.017	±0.004	±0.004

Table 2. Difference between band-averaged emissivity from laboratory spectra and emissivity from the MOD21 algorithm for bands 29, 30 and 31 in both studied sites. Results are obtained for both day ($\Delta\varepsilon_d$) and night ($\Delta\varepsilon_n$) sensor overpass.

	White Sands		Great Sands	
	$\Delta\varepsilon_d$	$\Delta\varepsilon_n$	$\Delta\varepsilon_d$	$\Delta\varepsilon_n$
B29	-0.017	-0.044	-0.036	-0.044
B31	0.008	0.012	-0.011	-0.013
B32	0.007	0.008	-0.002	-0.005

Table 3. Absolute value of the average difference between West and East LSEs for the same zenithal angle. Results are shown for the three MODIS thermal bands in both sites and for the two different sensor time overpasses.

	White Sands		Great Sands	
	Daytime	Nighttime	Daytime	Nighttime
B29	0.007	0.008	0.005	0.007
B31	0.0007	0.0007	0.002	0.002
B32	0.001	0.0002	0.0003	0.0004

Table 4. Average emissivity value and RSD for all the zenithal angles and maximum difference between nadir and off-nadir ($\Delta\varepsilon_\theta$) of the LSE for the MODIS bands 31 and 32 in both selected sites.

	White Sands		Great Sands	
	B31	B32	B31	B32
Average	0.958	0.968	0.948	0.969
RSD	±0.001	±0.0004	±0.002	±0.005
$\Delta\varepsilon_\theta$	0.003	0.001	0.001	0.002

List of Figure Captions

Figure 1. Geo-located Google Earth images showing of the two selected sites a) White Sands and b) Great Sands. Pictures of the two sites at ground level are shown.

Figure 2. Maps of graybody pixels (in black), corresponding to water or vegetation, and bare soil pixels (in white) for a) White Sands and b) Great Sands sites. The border of the two deserts is outlined in green. The 50-km circumference centered on the selected coordinates (blue point) is shown in red.

Figure 3. Maps of LST&E from the MOD21 simulated algorithm for White Sands, DOY 68, 2010 (left) and Great Sands, DOY 259, 2012 (right). The desert area is outlined and the 4 pixels used to obtain the LST&E are delimited by a blue square in both sites.

Figure 4. Comparison of MOD21 simulated LSE retrievals at near-nadir (2°-16°) for White Sands and Great Sands for day time (WS_MOD21_day and GS_MOD21_day) and nighttime (WS_MOD21_night and GS_MOD21_night) overpasses, with laboratory emissivity values for both sites (Hulley, personal communication) averaged to MODIS bands 29, 31 and 32. Uncertainties associated to MOD 21 LSEs were the average RSDs and uncertainties for the laboratory emissivity were provided by Dr. Hulley.

Figure 5. Zenithal variation of emissivity estimates from MODIS thermal bands over a) White Sands and b) Great Sand. Positive (negative) zenith angles correspond to East (West) azimuth angles. RSDs (see section 4) for each zenithal LSE value are shown as uncertainty bars.

Figure 6. Comparison of MOD21 LSE in band 29 for White Sands and Great Sands with predicted values calculated from Eqs. (14) and (15). Field emissivity measurements for a White Sands sample are also included.

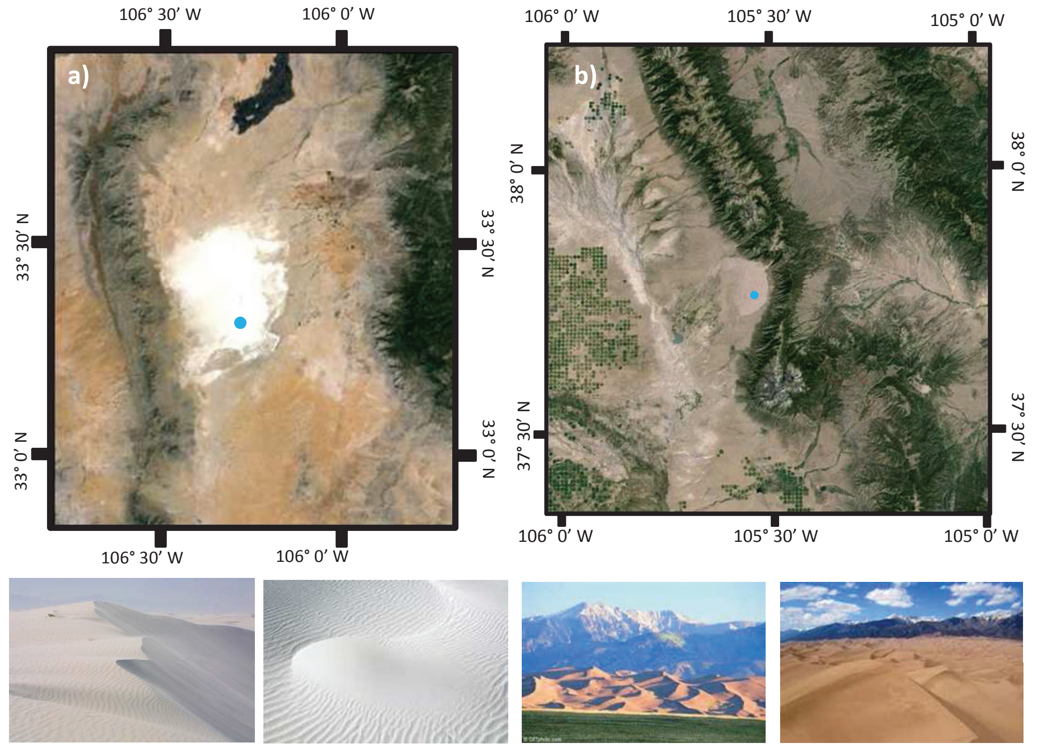

Figure 1. Geo-located Google Earth images showing of the two selected sites a) White Sands and b) Great Sands. Pictures of the two sites at ground level are shown.

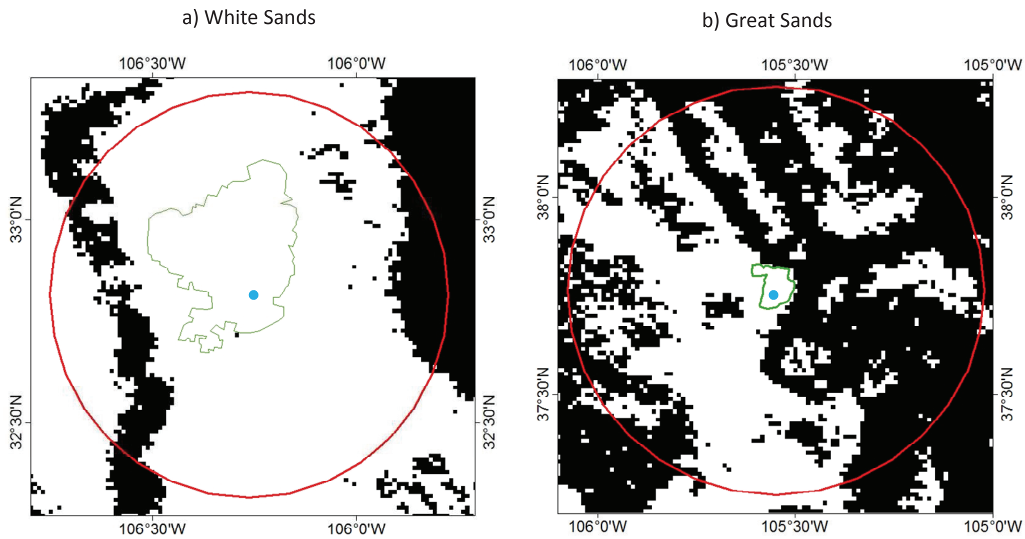

Figure 2. Maps of graybody pixels (in black), corresponding to water or vegetation, and bare soil pixels (in white) for a) White Sands and b) Great Sands sites. The border of the two deserts is outlined in green. The 50-km circumference centered on the selected coordinates (blue point) is shown in red.

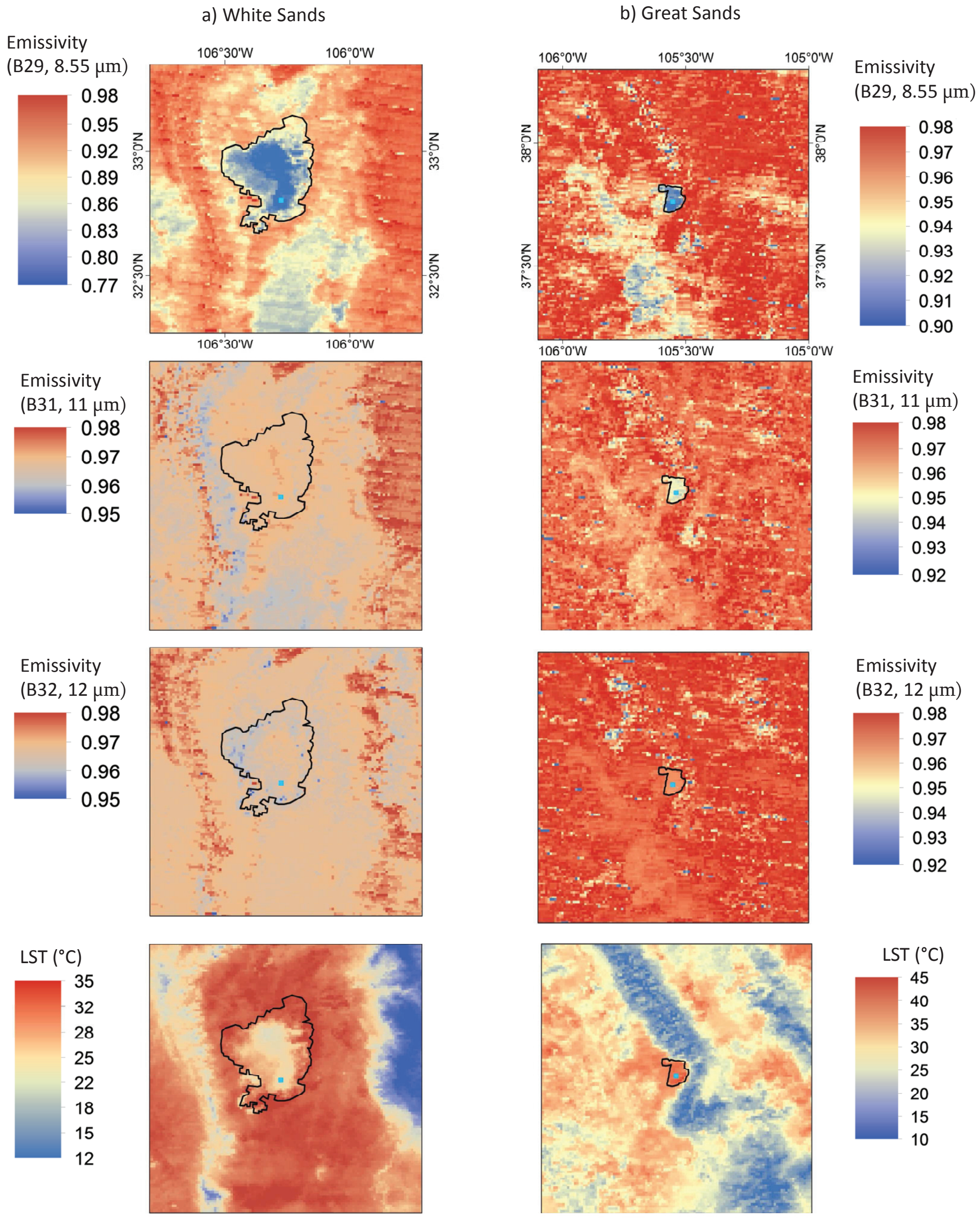

Figure 3. Maps of LST&E from the MOD21 simulated algorithm for White Sands, DOY 68, 2010 (left) and Great Sands, DOY 259, 2012 (right). The desert area is outlined and the 4 pixels used to obtain the LST&E are delimited by a blue square in both sites.

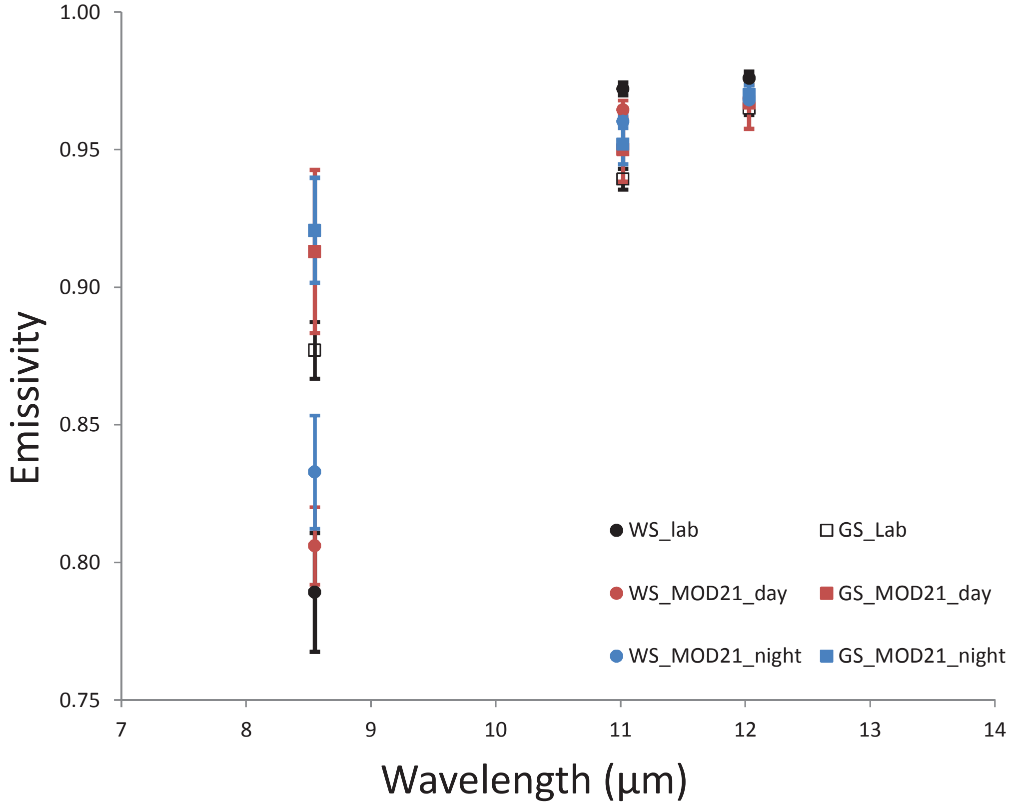

Figure 4. Comparison of MOD21 simulated LSE retrievals at near-nadir (2°-16°) for White Sands and Great Sands for day time (WS_MOD21_day and GS_MOD21_day) and nighttime (WS_MOD21_night and GS_MOD21_night) overpasses, with laboratory emissivity values for both sites (Hulley, personal communication) averaged to MODIS bands 29, 31 and 32. Uncertainties associated to MOD 21 LSEs were the average RSDs and uncertainties for the laboratory emissivity were provided by Dr. Hulley.

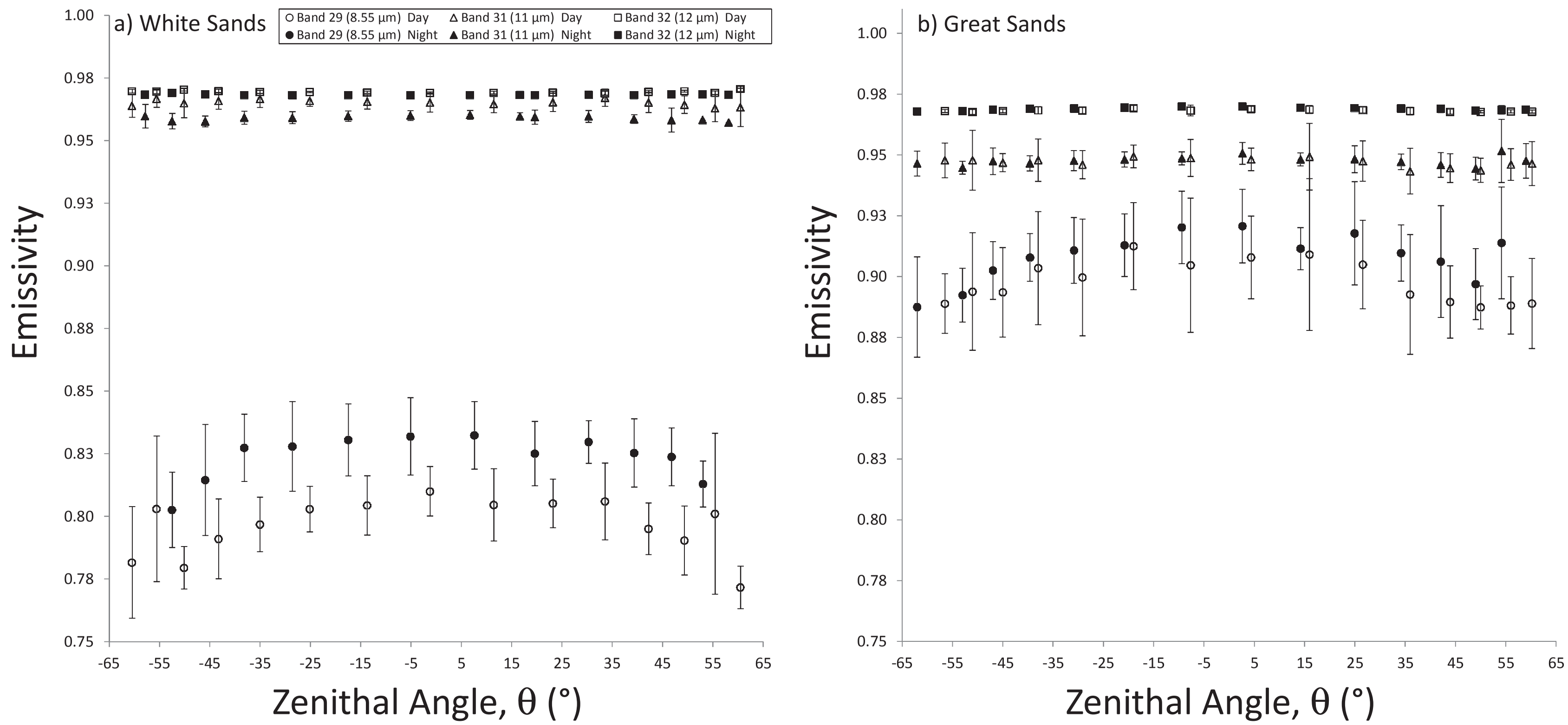

Figure 5. Zenithal variation of emissivity estimates from MODIS thermal bands over a) White Sands and b) Great Sand. Positive (negative) zenith angles correspond to East (West) azimuth angles. RSDs (see section 4) for each zenithal LSE value are shown as uncertainty bars.

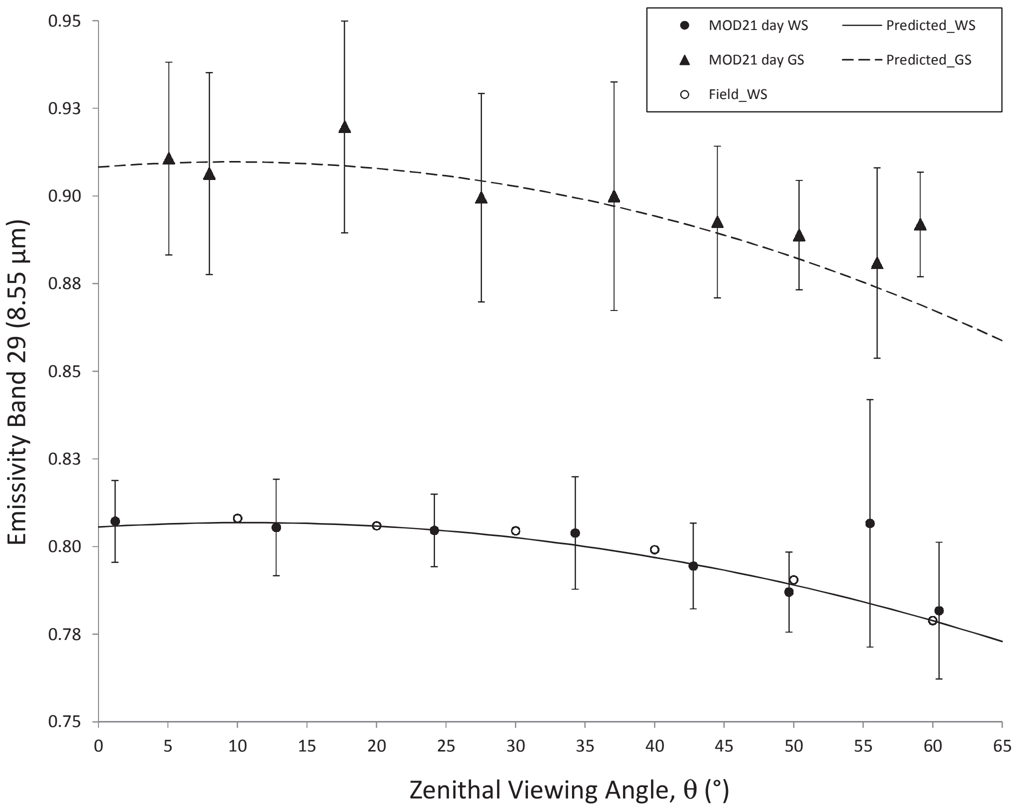

Figure 6. Comparison of MOD21 LSE in band 29 for White Sands and Great Sands with predicted values calculated from Eqs. (14) and (15). Field emissivity measurements for a White Sands sample are also included.